Article

Using ferrous-oxidizing bacteria to enhance the performance of a pH neutral all-iron flow battery

The Fe^{2+}-DTPA chamber in two-chamber system

*DTPA:Diethylenetriaminepentaacetic acid

Sitao Li, Sen Fan, Xinyuan Peng, Decong Zheng, Daping Li

lidp@cib.ac.cn

Highlights

Microaerobic FeOB can be rapidly enriched by electrochemical methods

FeOB improved output performance and electrochemical properties in half-battery

The specific capacity prominently increased in RFB by FeOB at 0.3 M, 10 mA/cm^2

Brucella was indicated as an electroactive FeOB, which is still undiscovered so far

Article

Using ferrous-oxidizing bacteria to enhance the performance of a pH neutral all-iron flow battery

Sitao Li,[1,2] Sen Fan,[1,3] Xinyuan Peng,[1,3] Decong Zheng,[1,2] and Daping Li[1,2,4,*]

SUMMARY

Among various redox flow batteries (RFBs), the all-iron RFBs have greater application potential due to high accessibility of electrolytes. However, the potential of microaerobic ferrous-oxidizing bacteria (FeOB) to improve the performance of RFB has been neglected. Here, several experiments were conducted using Fe^{2+}-diethylenetriaminepentaacetic acid (DTPA)/$Na_3[Fe(CN)_6]$ as a redox couple for investigating the enhanced performance by FeOB in this RFB. Results showed that the maximum current density of experimental reactors could achieve 22.56 A/m^2 at 0.1 M, whereas power density could still maintain 3.42 W/m^2 (16.96 A/m^2 and 1.58 W/m^2 for control group); meantime, the polarization impedance of anode increased slower and Fe^{2+}-DTPA oxidation peak emerged maximum 494 mV negative shift. With increased electrolyte concentration in chronopotentiometry experiments, the experimental reactor achieved higher discharging specific capacity at 0.3 M, 10 mA/cm^2. Microbial composition analysis showed maximum 75% is *Brucella*, indicating *Brucella* has ferrous-oxidizing electroactivity.

INTRODUCTION

Commonly used fossil fuels have caused severe climate change and environmental damage; there are growing calls to expand the use of renewable energy sources,[1] like solar energy.[2] However, the process of storing and utilizing the acquired energy is still under development. For most of the renewable energy sources (e.g., sun, tide), they are produced intermittently and can provide a large amount of energy in a short time, so it is difficult to meet the needs of continuous production and life of the urban population if not converted into electricity and stored in time.[3] Furthermore, because power plants are usually located in suburban areas, a large-capacity energy storage device is required for storage and scheduling to reduce the spatial and temporal gaps between energy and users.[4] Among the various options, redox flow batteries (RFBs) have distinct advantages in power storage compared with conventional batteries. They can withstand higher current charging/discharging and exhibit longer cycle lives.[5,6] Especially, the uncoupling of power density and capacity allows RFBs to have their separate reaction unit and external storage tanks, which enables scaling up of the power output and energy storage capacity independently for different kinds of demands.

Since the concept of RFBs was first proposed in 1974,[7] it has been widely investigated and applied in various fields. Currently, several metallic ions, such as vanadium,[8,9] chromium,[10] iron,[11] and zinc,[12] and metalloid elements, such as bromine[13] and sulfur,[14] are all being developed as alternatives to traditional lithium and lead-based batteries. However, a conventional redox pair composed of different elements can cause bidirectional transmission of ions; meantime, the slow reaction kinetics of ions can lead to severe hydrogen evolution reactions (HER). Therefore, all-iron RFBs are gradually attracting attention due to their low cost and better performance. However, as Fe^{3+} ions are easily hydrolyzed into insoluble $Fe(OH)_3$ precipitates under neutral to alkaline conditions, resulting in an irreversible loss of battery capacity, most of the redox pairs of existing all-iron RFBs adopted chelate forms of ferrous ion.[15] Several studies have tested a variety of iron chelators, including triethanolamine (TEA),[16] 3- [bis (2-hydroxyethyl)amino]-2-hydroxypropanesulphonic acid (DIPSO),[17] citrate,[18] and lots of other ligands, demonstrating the stability and redox reversibility under suitable conditions.[19] For many aqueous phase all-iron flow batteries, they use high concentrations of strong bases as the supporting electrolyte[20,21] (KOH or NaOH) to maintain a specific conductance and simultaneously control the decomposition of iron chelates. Diethylenetriaminepentaacetic acid (DTPA) is a highly effective chelating agent and exhibits a good electrochemical characteristic. In preliminary experiments, DTPA chelated iron shows a reversible $Fe^{2+/3+}$ system (0.469V vs. RHE, 1 mM) and a high solubility (maximum about 0.5 M) in neutral media (pH ≈ 7.0, 25°C).[22] Compared with other common chelating agents stabilized in weakly acidic environments (e.g., ethylenediaminetetraacetic acid, EDTA), $Fe^{2+/3+}$-DTPA is more stable and does not

[1]Key Laboratory of Environmental and Applied Microbiology, Environmental Microbiology Key Laboratory of Sichuan Province, Chengdu Institute of Biology, Chinese Academy of Science, Chengdu 610041, China
[2]University of Chinese Academy of Sciences, Beijing 100049, China
[3]Collage of Life Sciences, Sichuan University, Chengdu 610041, China
[4]Lead contact
*Correspondence: lidp@cib.ac.cn
https://doi.org/10.1016/j.isci.2023.108595

cause ion displacement at pH7. Besides, DTPA is also poorly biodegradable, suggesting that it cannot be utilized as a carbon source by microorganisms.

Nevertheless, to the best of our knowledge, the potential application of microorganisms for RFB enhancement is barely to be investigated; only a few studies existed up to now.[23,24] The bacteria involved in ferrous oxidation/reduction processes are widely distributed in various natural and artificial ecosystems, which cause various environmental problems such as acid mine wastewater emission[25,26] and iron structure corrosion.[27,28] Certain iron reduction bacteria such as *Geobacter* have been widely employed in the remediation of soil and groundwater.[29] The iron redox rate in biocatalytic processes is significantly higher than that in chemical catalytic processes. Over these years, a large number of electroactive bacteria have been discovered and used in the electrocatalytic processes involved in various fields. Several heterotrophic or facultative autotrophic iron reduction bacteria, such as *Escherichia coli* FR-2, can accept electrons from the cathode to reduce Fe^{3+}-EDTA. Moreover, the coculture with denitrifiers can efficiently remove absorbed NO,[30–32] suggesting a potential for bacteria to enhance the performance of all-iron RFBs. However, studies on neutral ferrous oxidizing bacteria (FeOB) remain scant, mainly due to their strict living environments. Compared with the *Thiobacillus ferrooxidans* found in strong acidic environments, neutral FeOB are predominantly found in near-neutral environments. In such conditions, the ferrous ion has a lower redox potential (+0.77 V at pH 2, $\pm$0.1 V at pH 7)[33] and forms precipitates of $Fe(OH)_3$ as an oxidation product, suggesting that these FeOB can only use nitrates or low concentrations of oxygen as the final electron acceptors in the respiratory chain. As a result, neutral microaerobic Fe^{2+} oxidizers are often restricted to live in areas accompanied with a high Fe^{2+} and low O_2 concentrations where the bio-oxidation rate can surpass the abiotic rate. However, because neutral microaerobic FeOB are difficult to isolate and purify, studies only focused on identification despite their abundance.[34]

In this study, an electrochemical method was used based on the conventional anaerobic gradient tube enrichment method,[35] to selectively enrich electroactive FeOB. The FeOB were grown on the surface of the graphite felt, with the Fe^{2+}-DTPA as the only energy source, and used for enhancing the performance of RFB. Two experimental reactors (R1, R2) and one control reactor (CK) were operated in batch experiments. For chronopotentiometry (GCD) experiments, only one experimental (GCD) and one control reactors (CK) were needed. The FeOB enrichment culture (10%) was introduced in experimental reactors as inoculum in the first batch of the batch experiments or GCD experimental cultivation process, whereas no microbial inoculum was added in CK. The contents of the anodic chambers were stirred using magnetic stirrers and kept at room temperature.

RESULT

The performance of half-batteries in batch experiments

In half-battery experiments, only the discharging process existed, which could intuitively reflect that the FeOB promoted the Fe^{2+}-DTPA oxidation rate compared with the simple chemical process. Before the 55th h, 200 Ω resistors were connected in series to restrict the current density and facilitated the microorganisms to attach to the graphite felt surface. A visible color change of electrolyte occurred before discharging (Figure S1A) and after discharging (Figure S1B), which mainly attributed to the progressive transfer of electrons; Fe^{2+}-DTPA (light yellow) was oxidized to Fe^{3+}-DTPA (dark red) whereas $[Fe(CN)]^{3-}$ (bright yellow) was reduced to $[Fe(CN)]^{4-}$ (light green). The current density and anodic potential for the batch experiments over time (external resistance load of 10 Ω) is shown in Figure 1A. At the end of period 1, the increasing current density in the experimental reactors indicated that the bacteria might colonize on the graphite felt successfully. Both experimental reactors (R1 and R2) exhibited similar and significantly higher maximum current densities (22.56 and 21.92 A/m², respectively) during period 2 compared with CK (16.96 A/m²). The maximum current density revealed a declining trend for CK, which may be attributed to membrane or electrode contamination. However, the current densities of R1 and R2 increased, peaked, and decreased during the whole process with the extension of time, which may be due to the growth of microorganisms and an increase in anode resistance.

The change in the anodic potential is related to the change in the current density, with the lowest initial potential of −133 mV for CK, compared with −173 mV and −179 mV for R1 and R2, respectively. The presence of FeOB accelerated the transfer of electrons from Fe^{2+}-DTPA to the anodes. This decreased the overpotential and led to a lower anodic potential, resulting in higher current output. Notably, in the last seven batches of period 2, the anodic potential of R1 and R2 was lower than that of CK, even throughout the discharging process. It is worth noting that the observed potential contraflexure might be due to the reduction of the anodic polarization, which is affected by the decrease in the output current.

The Coulombic efficiency and Fe^{2+}-DTPA oxidation rate were also recorded in Figure S2. For all three reactors, the Coulombic efficiency was maintained above 99% in all the batches. The oxidation rate reached up to maximum 99.2% (87.48%–99.2%) for R1 and 99.1% (80.0%–99.1%) for R2 compared with CK (96.75%; 75.32%–96.75%) excepted the 6th batch, suggesting that FeOB may increase the battery capacity. In batch experiments operation, each electrolyte replacement might bring about small changes in external environment (e.g., location of the magnetic stirrers) and therefore affect the internal resistance of half-battery, ultimately determining the oxidation rate.

To analyze the performance difference, polarization and power curves were determined at the end of each period. For period 1 (Figure 1B), the maximum power density achieved for (1) CK was 3.17 W/m², with a current density of 12.07 A/m²; (2) R1 was 3.53 W/m², with a current density of 13.76 A/m²; and (3) R2 was 3.41 W/m², with a current density of 13.17 A/m². In other words, the maximum output power densities for R1 and R2 were higher than that of CK. Compared with the period 1, the period 2 (Figure 1C) exhibited a much greater difference, with a maximum power density for (1) CK of 1.58 W/m², with a current density of 6.45 A/m²; (2) R1 of 3.42 W/m², with a current density of 13.39 A/m²; and (3) R2 of 3.12 W/m², with a current density of 12.85 A/m². After 10 batches of period 2, all three reactors exhibited a reduction in the maximum power density because of the rise in the internal resistance caused by membrane or electrode contamination. Nevertheless, the
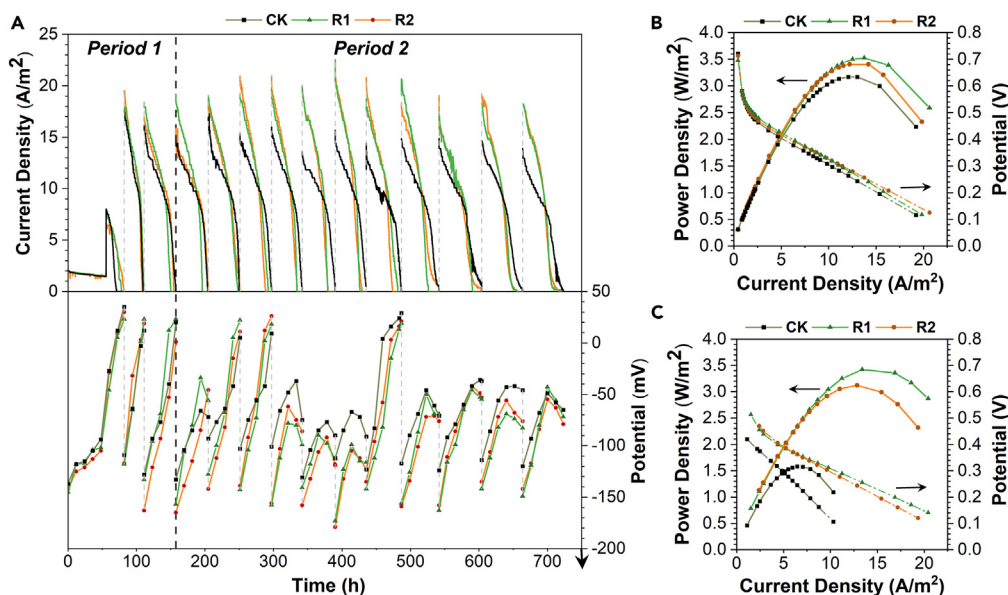
Figure 1. Output performance of half-battery discharging process

(A) Current density (A/m^2) and anodic potential (V) over time for batch experiments, the dashed line splits period 1 and 2.

(B and C) Power density and polarization curves obtained after the end of period 1 and 2. CK: control group, R1 and R2: experimental group.

maximum power density output of the two experimental reactors remained at 96.9% for R1 and 91.5% for R2 compared with period 1, whereas that of CK was reduced by 49.8%.

The internal resistance variation was estimated from the slope of the polarization curves in the region dominated by ohmic loss[36] (Figures 1B and 1C). For period 1, the internal resistances were estimated to be 35 Ω, 30 Ω, and 33 Ω for CK, R1, and R2, respectively. Similarly, for period 2, the internal resistances were estimated to be 61 Ω, 31 Ω, and 30 Ω for CK, R1, and R2, respectively. Compared with the significant increase in the internal resistance of CK, the internal resistance of R1 and R2 remained stable and even decreased at the end of period 2, indicating that the attachment of FeOB may reduce the rate of increase of the internal resistance in flow batteries.

The characterization of electrochemical properties

The anode electrochemical impedance spectroscopy (EIS) data were measured at the end of each period for the three reactors; the cyclic voltammetry (CV) data was measured only at the end of period 2. A three-electrode system was used for the experiments: both working and counter electrodes were graphite felt, and an Ag/AgCl electrode was used as the reference. Before every test, the electrolyte was renewed and kept static for 30 min. The equivalent circuit is shown in Figure S3. The ohmic, charge transfer, and finite diffusion resistances were obtained from the EIS curves.[37] The ohmic resistance (Rohm), obtained directly from the intersection of the EIS curve with the real axis, was affected by the parallel combination of the electronic (electrode and ionic) resistance in the electrolyte. The electrochemical polarization resistance (Rp), caused by the charge transfer process, was calculated from the distance between two intersections, which are the two points where the ends of the semicircular portion will be in contact with the real axis. The values of Rohm and Rp are shown in Table 1. At the end of period 1 (Figure 2A), the Rp of the R1 and R2 was significantly lower than CK, which indicated that the FeOB might promote the charge transfer process from Fe^{2+}-DTPA to the surface of electrode. For both periods (Figures 2A and 2B), the Rp increased for all three anodes over time, which may be attributed to graphite felt contamination. However, both R1 and R2 maintained a relatively low Rp; the increase in their Rohm may be attributed to the FeOB growth, influenced by the contact between Fe^{2+}-DTPA and the graphite fiber.

For the CV test (Figure 2C), the voltage window was set from −0.9 V to 0.9 V, and the scan rate was 0.005 V/s. Due to higher reactant concentration and resistance of the CMI-7000S membrane, both oxidation and reduction peaks showed a large shift compared with CV curve in

Table 1. The values of R_{ohm} and R_P in CK, R1, and R2 recorded from the end of two periods

	Period 1			Period 2		
	CK	R1	R2	CK	R1	R2
R_{ohm} (Ω)	1.55	0.72	0.68	1.06	1.66	1.13
R_P (Ω)	7.95	2.58	1.21	11.71	3.33	5.77
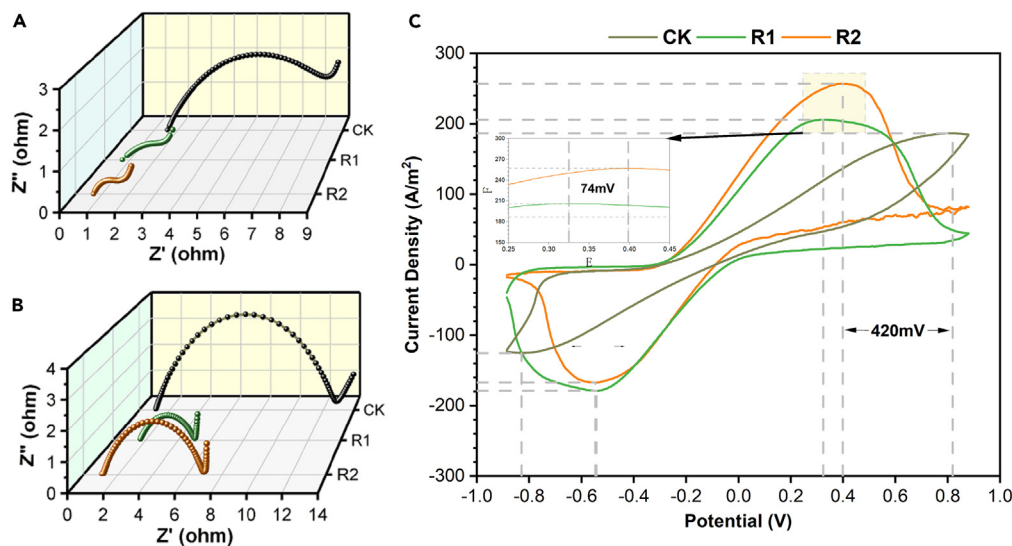
Figure 2. Electrochemical characteristics in half-battery experiments, including EIS and CV tests of anodes

(A and B) The 3D waterfall diagrams drawn from the EIS data obtained after period 1 and 2.

(C) CV curves variation after the whole batch experiments. Electrolyte was same as the 0.1 M initial electrolyte of the experiments. Both the working electrode and the counter electrode were graphite felt (2.5 × 2.5 × 0.3 cm^3); Ag/AgCl electrode was used as a reference. For EIS tests, frequency ranged from 100,000 to 0.01 Hz, and scan rate was 0.005 V/s and 15 s for measurement delay. For CV test, the scan rate was 0.005 V/s. CK: control group, R1 and R2: experimental group.

single-chamber condition, 1 mM Fe^{2+}-DTPA (Figure S4). Within the given voltage window, R1 and R2 showed similar reversible electrochemical behavior. The oxidation peak potentials of 0.1 M Fe^{2+}-DTPA for R1, R2, and CK were 325 mV, 399 mV, and 819 mV, whereas the experimental reactors showed a maximum 494 mV negative shift of the oxidation peak potential compared with CK. The corresponding oxidation peak current densities for R1 (206 A/m^2) and R2 (257 A/m^2) were much higher than that of CK (187 A/m^2), suggesting a stronger oxidative capacity in the presence of FeOB. Capacitance reflects the amount of charge stored in a capacitor; larger capacitance indicates higher charge content that can be utilized. Through CV curve integration, the capacitance of CK, R1, and R2, at the fixed voltage window (−0.9 V to 0.9 V) was 3.56 F, 7.72 F, and 6.69 F, respectively. The experimental reactors stored higher charge compared with the control reactor. The capacitance of R1 reached 2.71 times that of CK, demonstrating the potential of FeOB to achieve higher capacitance in RFBs.

The characterization through GCD experiments

The GCD experiments tested four performance parameters for three different reactant concentrations (0.1–0.5 M) by varying the current density (3–17 mA/cm^2), including Coulombic efficiency, energy efficiency, and charging/discharging specific capacity. The active area of the graphite electrodes was 6.25 cm^2. For the different reactant concentrations, 30 cycles were run consecutively using three progressively increasing current densities; each current density was run 10 cycles (Table 2). The charging/discharging cycles began with the charging process, and the required data were recorded and directly obtained from the battery formation/grading system. The Coulombic efficiency varied relatively large during the first 10 cycles but almost all of them maintaining more than 90%. The relatively low energy efficiency, related to the voltage efficiency, may be attributed to the nature of Fe^{2+}-DTPA. For a Fe^{2+}-DTPA concentration of 0.1 M, the experimental reactors exhibited larger specific capacities at all prescribed values of current density (Figure 3A).

However, the oscillation of the charging/discharging capacity at 3 mA/cm^2 caused a fluctuation in the Coulombic efficiency and energy efficiency, in the range of 87.9%–108.7%; a similar trend was observed for 0.3 M Fe^{2+}-DTPA at 10 mA/cm^2 (Figure 3B). This may be due to the fact that the biocatalytic process occurred only during the discharging process, which caused a large asymmetry in SOC change and thus lead to the fluctuation of Coulombic efficiency. The charging/discharging capacity increased during the first 10 cycles, and the average discharging capacity of GCD reached 1.37 times compared with CK, showing a prominent increase. In these two parts, a relatively low voltage

Table 2. The GCD experimental setup

Concentration (M)	Current density (mA/cm^2)	Total cycles (s)
0.1	3/5/7	30
0.3	10/12/15	30
0.5	13/15/17	30
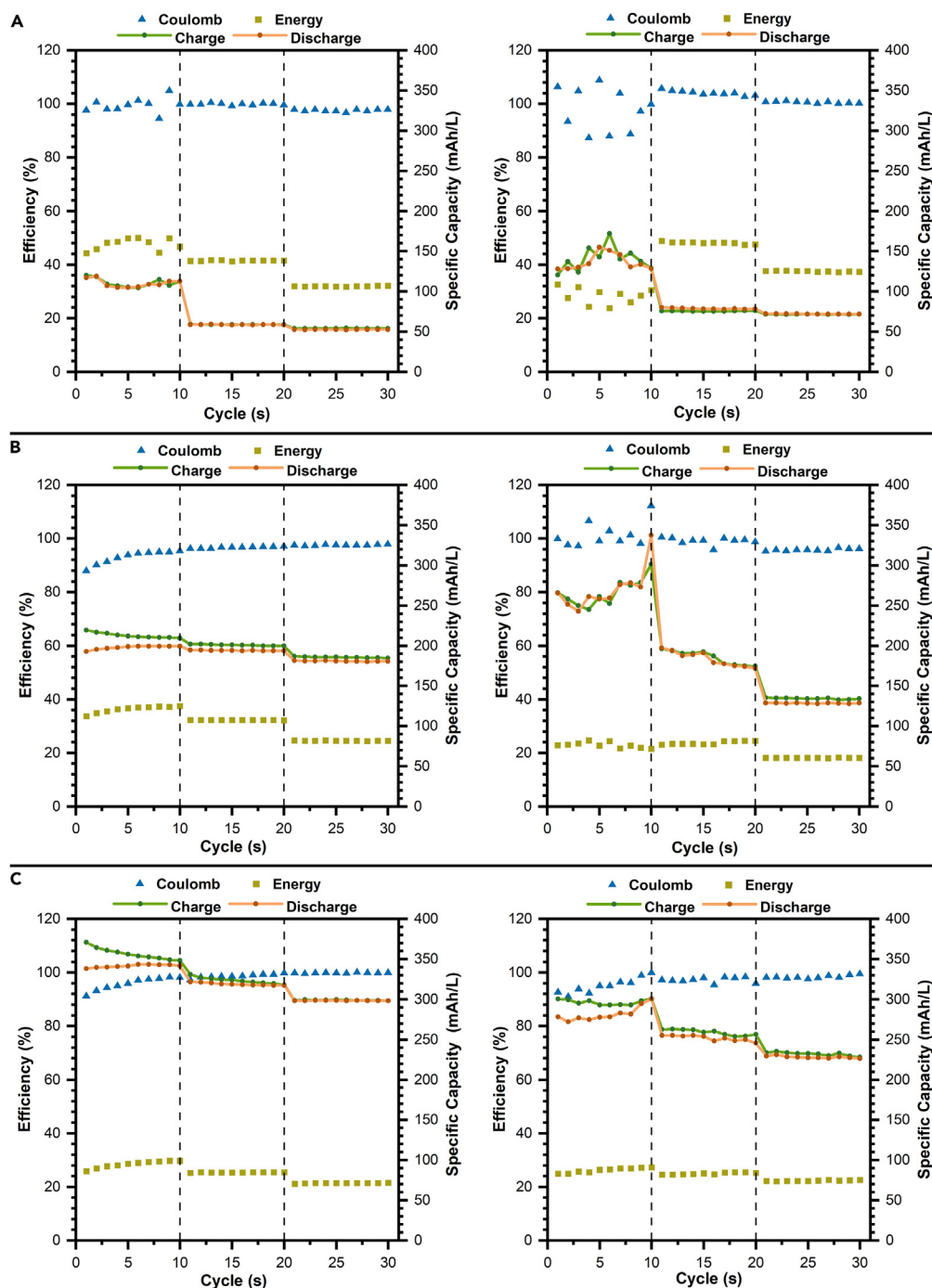
Figure 3. The Coulombic efficiency, energy efficiency, and charging/discharging specific capacity obtained from GCD experiments

(A) Fe^{2+}-DTPA concentration 0.1 M, current density 3, 5, 7 mA/cm^2.

(B) Fe^{2+}-DTPA concentration 0.3 M, current density 10, 12, 15 mA/cm^2.

(C) Fe^{2+}-DTPA concentration 0.5 M, current density 13, 15, 17 mA/cm^2. The left belongs to CK, and the right belongs to GCD. The dashed lines separate each 10 cycles. CK: control group, GCD: experimental group.

efficiency due to the growth of FeOB on the graphite felt surface increased the ohmic impedance to a certain extent; however, it had not yet started to serve as reducing polarization impedance, this may reflect the gradually adapting to the environment of FeOB. Nevertheless, as the current density continued to rise (over 10 mA/cm^2), the FeOB attachment did not increase the capacity compared with CK, irrespective of 0.3 M or 0.5 M Fe^{2+}-DTPA concentration (Figures 3B and 3C). The most obvious feature is that the discharging capacity of the first 10 cycles
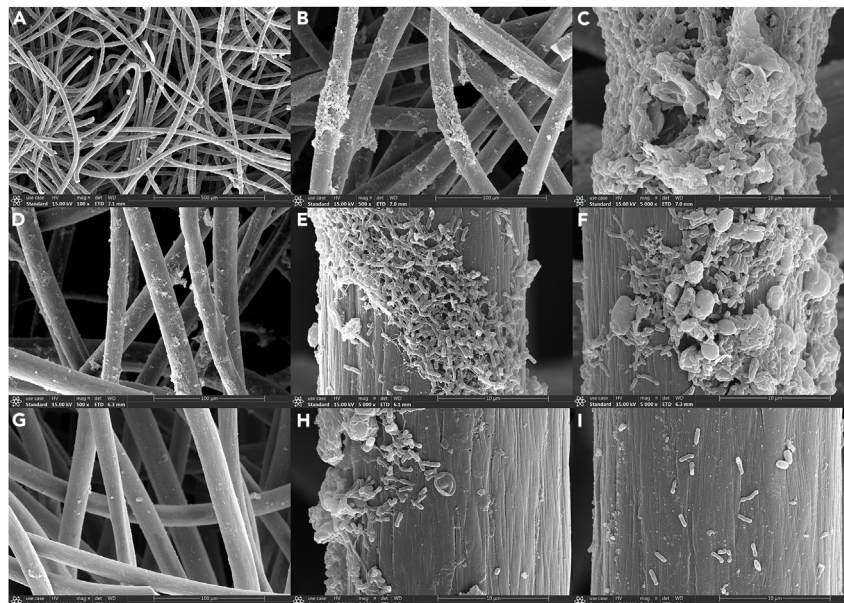
Figure 4. The SEM pictures of surface of the graphite felt
(A) The overall appearance took from R1 (100✕).
(B, D, and G) A closer observation of graphite fiber, took from R1, R2, and GCD, respectively (500✕).
(C, E, F, H, and I) Microbial communities attached to the surface of graphite fibers, took from R1, R2, and GCD, respectively (5000✕).

is lower than charging capacity, with the energy efficiency similar to that of CK. This phenomenon was speculated to occur due to the following reasons: (1) reactive oxide species (ROS) generated from fenton-like reactions by repeated high current charging and discharging, which damaged the cell structure; (2) possible toxicity of high Fe^{2+}-DTPA concentration toward FeOB; and (3) rapidly rising Na^+ concentration with increasing Fe^{2+}-DTPA concentration (32.14 g/L for 0.1 M, 113.96 g/L for 0.5 M, converted into NaCl), and may increase the effects of the first two terms. In future experiments, an independent cathode can be introduced for the Fe^{3+}-DTPA reduction process to maintain the FeOB activity.

The biofilm structure on the anode surface

At the end of period 2 and GCD experiments, a small piece of the bio-enhanced anode was removed for scanning electron microscope (SEM) observation. As shown in Figure 4, the microbial cells grew almost uniformly on the graphite fiber but did not form a dense biofilm covering the whole surface (Figure 4A). Magnified observations of the graphite fibers showed the attachment of microbial colonies in more detail (Figures 4B, 4D, and 4G).

The microbial colonies were more abundant in the batch experiments involving only the discharging process, in comparison to the GCD experimental graphite felt, which required both charging and discharging processes. This might be due to the toxic effect of high concentrations of Fe^{2+}-DTPA or microbial growth inhibition due to localized higher current densities. In addition, the H_2O_2 produced by the cyclic charging and discharging can trigger fenton-like reactions coupled with Fe^{2+}-DTPA, generating certain ROS, such as OH^- or O_2^-, which can harm the cytomembrane or DNA, thus lowering the microbial density. Largely rod-shaped and a few globular bacteria were found attached to the graphite felt surface (Figures 4C, 4E, 4F, and 4H), which secreted a large amount of extracellular polymeric substances (EPS) for tight attachment. In general, the relatively uniform and thin biofilm on the graphite felt ensured minimal influence on the mass transfer process.

The microbial community composition of the biofilm

At the end of period 2 and GCD experiments, the collected bio-anode and enrichment samples were sent for further microbial community analysis, each reactor or enrichment ("E" in Figure 5) repeated twice.

The community bar graph shows specific proportion on genus level (Figure 5A). For the two reactors of the batch experiments, *Brucella* was the dominant genus, reaching up to approximately 75.0% in R1. The other relatively abundant genera were *Acinetobacter* (18.4%), *Rhodococcus* (8.9%), *Alcaligenes* (3.8%), and *Flaviflexus* (5.5%). In comparison, the predominant FeOB genera in enrichment culture were *Dysgonomonas* (23.8%), *Azospirillum* (20.9%), *Comamonas* (19.5%), and unclassified *Enterobacteriaceae* (14.1%), with *Brucella* accounting only for 6.6%. Nevertheless, due to the inadequate understanding of microbial Fe^{2+} oxidation process, few studies have demonstrated that the bacteria obtained from enrichment culture can gain energy from the oxidation of Fe^{2+}, like photo-autotrophy[38] or detoxification by Fe^{2+} oxidation.[39] The vast difference among these microbial community compositions indicated that the dominant bacteria exhibited both
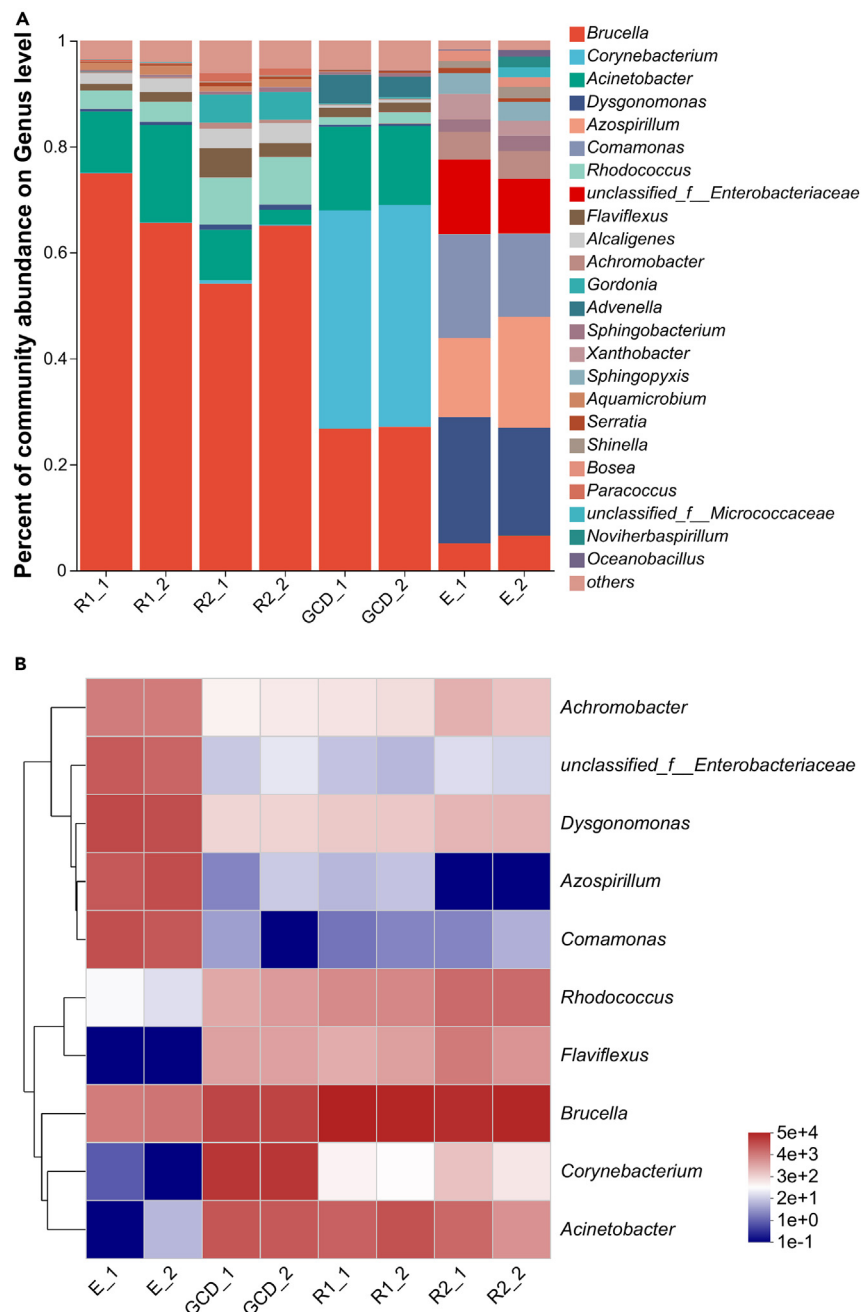
Figure 5. Microbial community analysis of graphite felt

(A) The bar plot of microbial community composition for E, R1, R2, and GCD.

(B) The community heatmap for E, R1, R2, and GCD. E: enrichment culture; R1 and R2: batch experimental group; GCD: GCD experimental group.

the ability to oxidize Fe^{2+} and electroactivity. For R1, R2, and GCD, the abundance of *Acinetobacter*, *Rhodococcus*, and *Flaviflexus* was bigger, except *Brucella*, compared with enrichments (Figure 5B). All genera were facultative autotrophic and facultative aerobic, and a variety of electron donors and electron acceptors can be used for cellular respiration. Therefore, the observed genera were speculated to have the capacity for Fe^{2+} oxidation. Compared with R1 and R2, the microbial community composition of GCD showed a maximum 41.9% *Corynebacterium* and 5.5% *Advenella* additionally, which might originate from the concomitant iron-reducing bacteria in inoculum. The *Corynebacterium* has been proven to exhibit the iron-reducing ability,[40] and the *Advenella* was shown to have a potential for the same.[41]

Brucella, as the culprit of brucellosis, is a kind of intracellular facultative parasitic bacteria for mammals and have been studied as a pathogen for many years. When introduced into the animal, *Brucella* can resist phagocytosis and digestion by macrophages, resulting in a

persistent infection. The main symptoms include fever and muscle aches; therefore, the study on its autotrophic ability has been neglected. In this study, on the basis of evidence that *Brucella* may have the ability of Fe^{2+} oxidation and electroactivity from experiments, some reasonable inferences about the mechanism for its Fe^{2+}-oxidizing function are made. Iron is a component of various proteins (e.g., Fe-S center), but in mammalian hosts, it often exists in a bound state. Therefore, the mammalian hosts considered it as a metal-restricted environment for *Brucella*.[42] As a result, *Brucella* has evolved efficient iron transporters located at the outer membrane, especially aimed at $Fe^{2+/3+}$-chelates, compared with other non-parasitic species. Bacterioferritin, a protein with a heme group, is potentially involved in the Fe^{2+}-DTPA oxidation process. Although the specific function of bacterioferritin has not yet been studied thoroughly,[43] it has a proven ability to reduce ferric hydroxide, with reductive NADH as the electron donor.[44,45] According to conjecture, the bacterioferritin possessed by *Brucella* can transfer electrons backward from Fe^{2+}-DTPA to NADH, coupling to the respiratory chain and finally transferring the electrons to electrode. Furthermore, *Brucella* as a facultative parasite possesses more catalase and/or superoxide dismutase (SOD) expression quantity as it needs to resist oxidative stress caused by macrophages.[46,47] This reason explains the strong resistance of *Brucella* to ROS attack.

At present, most of the found FeOB predominantly belong to the category of β-proteobacteria, with a few belonging to δ-proteobacteria.[48] However, *Acinetobacter* and *Brucella* are γ-proteobacteria and α-proteobacteria, respectively (Figure S5). Although their iron oxidation mechanism may not be the same as that of conventional FeOB,[49] they are still capable of obtaining energy through Fe^{2+} oxidation under given conditions at neutral pH and thus can be classified as neutral FeOB. This finding broadens the definition of FeOB. Because of the technical difficulties in purifying the found previously neutral microaerobic FeOB, they have not yet been employed in applications. However, the *Brucella* is easy to purify and has electroactive properties, indicating its potential as a FeOB for electrochemical applications involving iron oxidation.

DISCUSSION

In this study, the increasing current density and relatively lower anodic potential in the half-battery batch experiments prominently manifest the enhancement of FeOB on the Fe^{2+}-DTPA/Na_3[Fe(CN)$_6$] battery output. Compared with CK, the maximum power density of R1 and R2 decreased only slightly, with R1 maintaining a value of 3.42 W/m^2 after period 2. The EIS data indicated that the attachment of FeOB reduced the polarization resistance of graphite felt during the discharging process. The CV curves proved that the FeOB negatively shifted the oxidation peak potential of Fe^{2+}-DTPA, which may favor its oxidation speed. The GCD experiments showed that for a current density of 10 mA/cm^2 and Fe^{2+}-DTPA concentration of 0.3 M, FeOB significantly enhanced the charging/discharging capacity, whereas it reduced energy efficiency. However, the constant current charging/discharging results for higher current densities and Fe^{2+}-DTPA concentrations were not satisfactory due to ROS and high Fe^{2+}-DTPA and Na^+ concentrations. But for practical battery usage, continuous and constantly high current charging and discharging processes are not required, and therefore, the FeOB can adapt to higher Fe^{2+}-DTPA concentrations and perform better. In future works, we will configure a three-chamber reactor and introduce ferric reduction bacteria (FeRB) and allow the iron redox process to occur at two different electrodes, to avoid the mutual interference between the FeOB and FeRB and maintain the good performance. Furthermore, some new electrode materials should also be tested to improve the relatively low energy efficiency in all-iron RFB. The SEM pictures clearly presented the attachment and growth of FeOB on graphite fibers, indirectly suggesting that they can obtain energy from the Fe^{2+}-DTPA oxidation, whereas the graphite felt as an electron acceptor. The microbial composition analysis revealed the *Brucella* to be the most abundant genus, with maximum 75.0%. Through this study, we speculated the reasons for the strong capacity of *Brucella* to oxidize iron and resist ROS and classified it as a FeOB from this perspective. Meanwhile, we consider that in condition of using mixed culture as the inoculum, some of the existed heterotrophic/facultative heterotrophic bacteria may cause reversible side reactions involving the interconversion between organic matter and electrons, which can be reduced by using pure bacteria strain. Because of the technical difficulties in purifying microaerophilic neutral FeOB found previously, no cases have shown that this kind of FeOB has been put into use. However, the *Brucella* is easy to purify and also electroactive. This indicates its potential as FeOB for reducing the possibility of side reactions in RFB, and further electrochemical applications involved iron oxidation.

Limitations of the study

Because high concentrations of Fe^{2+}-DTPA can lead to higher salinity, and thus affect microbial cell growth, some microbial viability tests can be conducted to find the maximum survivability concentration and predict the maximum capacity of this battery. The ROS produced by constant current charging/discharging process will affect the microbial activity and therefore reduce the battery performance. But in regular battery usage, there is no need for a continuously and constantly high current charge/discharge process, and this all-iron RFB may perform better. Moreover, interactions among the microorganisms may also affect performance. Therefore, the pure *Brucella* can be used as inoculum in subsequent experiments.

STAR★METHODS

Detailed methods are provided in the online version of this paper and include the following:

- KEY RESOURCES TABLE
- RESOURCE AVAILABILITY
  - Lead contact
  - Materials availability

SUPPLEMENTAL INFORMATION

ACKNOWLEDGMENTS

AUTHOR CONTRIBUTIONS

S.L.: data curation, investigation, visualization, formal analysis, writing—original draft, writing—review & editing. S.F.: investigation, visualization. X.P.: investigation, visualization. D.Z.: investigation, visualization, formal analysis. D.L.: funding acquisition, conceptualization, project administration, resources, supervision, writing—review and editing.

DECLARATION OF INTERESTS

The authors declare that they have no known competing financial interests or personal relationships that could have appeared to influence the work reported in this paper.

REFERENCES

1. Singh, S., and Ru, J. (2022). Accessibility, affordability, and efficiency of clean energy: a review and research agenda. Environ. Sci. Pollut. Res. Int. 29, 18333–18347.
2. Izam, N.S.M.N., Itam, Z., Sing, W.L., and Syamsir, A. (2022). Sustainable Development Perspectives of Solar Energy Technologies with Focus on Solar Photovoltaic-A Review. Energies 15, 2790.
3. Ji, M., Zhang, W., Xu, Y., Liao, Q., Jaromír Klemeš, J., and Wang, B. (2023). Optimisation of multi-period renewable energy systems with hydrogen and battery energy storage: A P-graph approach. Energy Convers. Manag. 281, 116826.
4. Zhang, J., Du, K., Liu, J., Wang, Y., Zhang, W., and Yuan, J. (2023). The economic impact of energy storage co-deployment on renewable energy in China. J. Renew. Sustain. Energy 15, 035905.
5. Ravikumar, M.K., Rathod, S., Jaiswal, N., Patil, S., and Shukla, A. (2017). The renaissance in redox flow batteries. J. Solid State Electrochem. 21, 2467–2488.
6. Arévalo-Cid, P., Dias, P., Mendes, A., and Azevedo, J. (2021). Redox flow batteries: a new frontier on energy storage. Sustain. Energy Fuels 5, 5366–5419.
7. Thaller, L.H. (1977). REDOX FLOW BATTERIES. J. Electrochem. Soc. 124, C278–C279.
8. Li, L., Kim, S., Wang, W., Vijayakumar, M., Nie, Z., Chen, B., Zhang, J., Xia, G., Hu, J., Graff, G., et al. (2011). A Stable Vanadium Redox-Flow Battery with High Energy Density for Large-Scale Energy Storage. Adv. Energy Mater. 1, 394–400.
9. Satola, B. (2021). Review-Bipolar Plates for the Vanadium Redox Flow Battery. J. Electrochem. Soc. 168, 060503.
10. Bae*, C., Roberts, E.P.L., Chakrabarti, M.H., and Saleem, M. (2011). All-Chromium Redox Flow Battery for Renewable Energy Storage. Int. J. Green Energy 8, 248–264. Pii 934635669.
11. Gong, K., Xu, F., Grunewald, J.B., Ma, X., Zhao, Y., Gu, S., and Yan, Y. (2016). All-Soluble All-Iron Aqueous Redox-Flow Battery. ACS Energy Lett. 1, 89–93.
12. Li, B., Nie, Z., Vijayakumar, M., Li, G., Liu, J., Sprenkle, V., and Wang, W. (2015). Ambipolar zinc-polyiodide electrolyte for a high-energy density aqueous redox flow battery. Nat. Commun. 6, 6303.
13. Weng, G.-M., Li, Z., Cong, G., Zhou, Y., and Lu, Y.-C. (2017). Unlocking the capacity of iodide for high-energy-density zinc/polyiodide and lithium/polyiodide redox flow batteries. Energy Environ. Sci. 10, 735–741.
14. Zhang, S., Guo, W., Yang, F., Zheng, P., Qiao, R., and Li, Z. (2019). Recent Progress in Polysulfide Redox-Flow Batteries. Batter. Supercaps 2, 627–637.
15. Dinesh, A., Olivera, S., Venkatesh, K., Santosh, M.S., Priya, M.G., Inamuddin, Asiri, A.M., Asiri, A.M., and Muralidhara, H.B. (2018). Iron-based flow batteries to store renewable energies. Environ. Chem. Lett. 16, 683–694.
16. Lê, A., Floner, D., Roisnel, T., Cador, O., Chancelier, L., and Geneste, F. (2019). Highly soluble Fe(III)-triethanolamine complex relevant for redox flow batteries. Electrochim. Acta 301, 472–477.
17. Shin, M., Noh, C., Chung, Y., and Kwon, Y. (2020). All iron aqueous redox flow batteries using organometallic complexes consisting of iron and 3- bis (2-hydroxyethyl)amino -2-hydroxypropanesulfonic acid ligand and ferrocyanide as redox couple. Chem. Eng. J. 398, 125631.
18. Song, Y., Zhang, K., Li, X., Yan, C., Liu, Q., and Tang, A. (2021). Tuning the ferrous coordination structure enables a highly reversible Fe anode for long-life all-iron flow batteries. J. Mater. Chem. A Mater. 9, 26354–26361.
19. Hawthorne, K.L., Wainright, J.S., and Savinell, R.F. (2014). Studies of Iron-Ligand Complexes for an All-Iron Flow Battery Application. J. Electrochem. Soc. 161, A1662–A1671.

20. Liu, X., Li, T., Yuan, Z., and Li, X. (2022). Low-cost all-iron flow battery with high performance towards long-duration energy storage. J. Energy Chem. 73, 445–451.

21. Shin, M., Noh, C., and Kwon, Y. (2023). Electrolyte optimization of alkaline aqueous redox flow battery using iron-2,2-bis(hydroxymethyl)-2,2',2'-nitrilotriethanol complex as active material for anolyte. Chem. Eng. J. 453, 139738.

22. Waters, S.E., Robb, B.H., and Marshak, M.P. (2020). Effect of Chelation on Iron-Chromium Redox Flow Batteries. ACS Energy Lett. 5, 1758–1762.

23. Santos, M.S., Peixoto, L., Azevedo, J., Monteiro, R.A., Dias-Ferreira, C., Alves, M.M., and Mendes, A. (2020). Microbially-charged electrochemical fuel for energy storage in a redox flow cell. J. Power Sources 445, 227307.

24. Santos, M.S., Peixoto, L., Mushtaq, K., Dias-Ferreira, C., Mendes, A., and Alves, M.M. (2021). Bioelectrochemical energy storage in a Microbial Redox Flow Cell. J. Energy Storage 39, 102610.

25. Su, Z., Li, X., Xi, Y., Xie, T., Liu, Y., Liu, B., Liu, H., Xu, W., and Zhang, C. (2022). Microbe-mediated transformation of metal sulfides: Mechanisms and environmental significance. Sci. Total Environ. 825, 153767.

26. Kang, J.X., and Wang, Y.Y. (2022). The role of Acidithiobacillus ferrooxidans in Fe(II) oxidation of pyrite in bioleaching processes. J. Chem. Technol. Biotechnol. 97, 2013–2023.

27. Wang, H., Hu, C., Zhang, L., Li, X., Zhang, Y., and Yang, M. (2014). Effects of microbial redox cycling of iron on cast iron pipe corrosion in drinking water distribution systems. Water Res. 65, 362–370.

28. Wang, J., Sickinger, M., Ciobota, V., Herrmann, M., Rasch, H., Rösch, P., Popp, J., and Küsel, K. (2014). Revealing the microbial community structure of clogging materials in dewatering wells differing in physico-chemical parameters in an open-cast mining area. Water Res. 63, 222–233.

29. Nazir, A., Jubeen, F., Sultan, M., Ala Khurram, A., Abdul Latif, A., Altaf, I., Ibrahim, S.M., Iqbal, M., and Nazir, A. (2023). Environmental remediation and generation of green electricity using constructed wetlands coupled with microbial fuel cell model system. Arab. J. Chem. 16, 104941.

30. Zhao, J., Zhang, C., Sun, C., Li, W., Zhang, S., Li, S., and Zhang, D. (2018). Electron transfer mechanism of biocathode in a bioelectrochemical system coupled with chemical absorption for NO removal. Bioresour. Technol. 254, 16–22.

31. Xia, Y., Zhao, J., Li, M., Zhang, S., Li, S., and Li, W. (2016). Bioelectrochemical Reduction of Fe(II)EDTA-NO in a Biofilm Electrode Reactor: Performance, Mechanism, and Kinetics. Environ. Sci. Technol. 50, 3846–3851.

32. Zhao, J., Feng, K., Liu, S.-H., Lin, C.-W., Zhang, S., Li, S., Li, W., and Chen, J. (2020). Kinetics of biocathodic electron transfer in a bioelectrochemical system coupled with chemical absorption for NO removal. Chemosphere 249, 126095.

33. Keffer, J.L., McAllister, S.M., Garber, A.I., Hallahan, B.J., Sutherland, M.C., Rozovsky, S., and Chan, C.S. (2021). Iron Oxidation by a Fused Cytochrome-Porin Common to Diverse Iron-Oxidizing Bacteria. mBio 12. e01074-21.

34. Prokaryotes (2006). A Handbook on the Biology of Bacteria, Vol 5, Third Edition.

35. Emerson, D., Field, E.K., Chertkov, O., Davenport, K.W., Goodwin, L., Munk, C., Nolan, M., and Woyke, T. (2013). Comparative genomics of freshwater Fe-oxidizing bacteria: implications for physiology, ecology, and systematics. Front. Microbiol. 4, 254.

36. Logan, B.E., Hamelers, B., Rozendal, R., Schröder, U., Keller, J., Freguia, S., Aelterman, P., Verstraete, W., and Rabaey, K. (2006). Microbial fuel cells: Methodology and technology. Environ. Sci. Technol. 40, 5181–5192.

37. Pezeshki, A.M., Sacci, R.L., Delnick, F.M., Aaron, D.S., and Mench, M.M. (2017). Elucidating effects of cell architecture, electrode material, and solution composition on overpotentials in redox flow batteries. Electrochim. Acta 229, 261–270.

38. Heising, S., and Schink, B. (1998). Phototrophic oxidation of ferrous iron by a Rhodomicrobium vannielii strain. Microbiol Ser (N. Y.) 144, 2263–2269.

39. Kamnev, A.A., Tugarova, A.V., Shchelochkov, A.G., Kovács, K., and Kuzmann, E. (2020). Diffuse reflectance infrared Fourier transform (DRIFT) and Mossbauer spectroscopic study of Azospirillum brasilense Sp7: Evidence for intracellular iron(II) oxidation in bacterial biomass upon lyophilisation. Spectrochim. Acta Mol. Biomol. Spectrosc. 229, 117970.

40. Müller, F., Rapp, J., Hacker, A.-L., Feith, A., Takors, R., and Blombach, B. (2020). CO_2/HCO_3^- Accelerates Iron Reduction through Phenolic Compounds. mBio 11, e00085-20.

41. Matsuoka, M., Park, S., An, S.-Y., Miyahara, M., Kim, S.-W., Kamino, K., Fushinobu, S., Yokota, A., Wakagi, T., and Shoun, H. (2012). Advenella faeciporci sp nov., a nitrite-denitrifying bacterium isolated from nitrifying-denitrifying activated sludge collected from a laboratory-scale bioreactor treating piggery wastewater. Int. J. Syst. Evol. Microbiol. 62, 2986–2990.

42. Roop, R.M., II (2012). Metal acquisition and virulence in Brucella. Anim. Health Res. Rev. 13, 10–20.

43. Smith, J.L. (2004). The physiological role of ferritin-like compounds in bacteria. Crit. Rev. Microbiol. 30, 173–185.

44. Pullin, J., Bradley, J.M., Moore, G.R., Le Brun, N.E., Wilson, M.T., and Svistunenko, D.A. (2021). Electron Transfer from Haem to the Di-Iron Ferroxidase Centre in Bacterioferritin. Angew. Chem., Int. Ed. Engl. 60, 8376–8379.

45. Steunou, A.S., Vigouroux, A., Aumont-Nicaise, M., Plancqueel, S., Boussac, A., Ouchane, S., and Moréra, S. (2022). New insights into the mechanism of iron transport through the bacterial Ftr system present in pathogens. FEBS J. 289, 6286–6307.

46. Jacob, J., Finke, A., and Mielke, M. (2020). Survival of Brucella abortus S19 and other Brucella spp. in the presence of oxidative stress and within macrophages. Folia Microbiol. 65, 879–894.

47. Martinez, M., Ugalde, R.A., and Almiron, M. (2006). Irr regulates brucebactin and 2,3-dihydroxybenzoic acid biosynthesis, and is implicated in the oxidative stress resistance and intracellular survival of Brucella abortus. Microbiol Ser (N. Y.) 152, 2591–2598.

48. Feng, S., Jiang, Y., Cai, Z., Zeng, Y., and Zhou, J. (2019). The State of Arts:Sources,Microbial Processes and Ecological Effects of Iron in the Marine Environment. Adv. Earth Sci. 34, 513–522.

49. Quatrini, R., Appia-Ayme, C., Denis, Y., Jedlicki, E., Holmes, D.S., and Bonnefoy, V. (2009). Extending the models for iron and sulfur oxidation in the extreme Acidophile Acidithiobacillus ferrooxidans. BMC Genom. 10, 394.

50. Wolin, E.A., Wolin, M.J., and Wolfe, R.S. (1963). FORMATION OF METHANE BY BACTERIAL EXTRACTS. J. Biol. Chem. 238, 2882–2886.

51. Emerson, D., and Floyd, M.M. (2005). Enrichment and isolation of iron-oxidizing bacteria at neutral pH. In Environmental Microbiology, J.R. Leadbetter, ed., pp. 112–123.

STAR★METHODS

KEY RESOURCES TABLE

REAGENT or RESOURCE	SOURCE	IDENTIFIER
Biological samples		
Initial ferrous-oxidizing bacteria (FeOB) sample	Natural Rust	N/A
Chemicals, peptides, and recombinant proteins		
Diethylenetriaminepentaacetic acid (DTPA)	Nanjing BioDuly	CAS: 67-43-6
Fe^{3+}-DTPA (disodium salt)	Nanjing BioDuly	CAS: 19529-38-5
$FeCl_2 \cdot 4H_2O$	Jingdongtianzheng Precision Chemical Reagent	CAS: 13478-10-9
$Na_3[Fe(CN)_6]$	Jingdongtianzheng Precision Chemical Reagent	CAS: 14217-21-1
$Na_4[Fe(CN)_6] \cdot 3H_2O$	Tianjin Fuchen	CAS: 14459-95-1
Graphite felt (3 mm)	Taiwan CeTech	GF030
CMI-7000S cation exchange membrane	Membrane International	CXM-200S (CMI-7000S)
Nafion™212 proton exchange membrane	Chemours	NR212
Deposited data		
16S rRNA high-throughput sequencing raw data	Mendeley Data	https://doi.org/10.17632/n8x6nrkg2y.2
Software and algorithms		
ZView	AMETEK	https://www.ameteksi.com/products/software/zview-software-en
OriginPro 2022	OriginLab	https://www.originlab.com/2022C

RESOURCE AVAILABILITY

Lead contact

Further information and requests for resources and reagents should be directed to and will be fulfilled by the lead contact, Daping Li (lidp@cib.ac.cn).

Materials availability

This study did not generate new unique reagents.

Data and code availability

- Data: For 16S rRNA high-throughput sequencing raw data, the datasets supporting the current study have been deposited and publicly accessible in Mendeley Data, https://doi.org/10.17632/n8x6nrkg2y.2.
- Code: This paper does not report original code.
- Other items: No other new unique reagent was generated. Any additional information required to reanalyze the data reported in this paper is available from the lead contact upon request.

EXPERIMENTAL MODEL AND STUDY PARTICIPANT DETAILS

This work did not need any unique experimental model.

METHOD DETAILS

Chemicals

DTPA (99.5%), Fe^{3+}-DTPA disodium salt (99.5%) were obtained from Nanjing BioDuly Co. (Nanjing, China). $FeCl_2 \cdot 4H_2O$ (99.7%), $Na_3[Fe(CN)_6]$ (99.5%) were obtained from Tianjin Jingdongtianzheng Precision Chemical Reagent Co. (Tianjin, China). $Na_4[Fe(CN)_6] \cdot 3H_2O$ (99.5%) was obtained from Tianjin Fuchen Co. (Tianjin, China). Ar (99.999%) was obtained from Chengdu Qiaoyuan Gas Co. (Chengdu, China). Graphite electrodes (3 mm thickness, spectral grade) was obtained from Taiwan CeTech Co. (Taiwan, China). CMI-7000S cation exchange membrane was obtained from Membrane International Inc. (USA). Nafion™212 membrane was obtained from Chemours Inc. (USA). All other chemicals were of analytical grade and used without further purification.

The allocation of 100% and 50% state of charge (SOC) Fe^{2+}-DTPA and $Na_3[Fe(CN)_6]$ solutions

Inorganic medium and phosphate buffer for the Fe^{2+}-DTPA electrolyte were composed of the components as follows (g per liter, final concentration): NH_4Cl, 1.50; $MgSO_4$, 0.20; $CaCl_2$, 0.10; $NaHCO_3$, 1.20; KH_2PO_4, 4.84; K_2HPO_4, 8.54; and additional 11.70 g/L NaCl serving as supporting electrolyte. Mineral solution and vitamin solution,[50] with a final concentration of 1 mL/L, was prepared to promote bacterial growth. The Fe^{2+}-DTPA complexes were prepared according to the following process: appropriate amount of DTPA and fivefold NaOH was added (e.g., 0.1 M DTPA and 0.5 M NaOH for 0.1 M concentration electrolyte) in deionized water (80% volume of the total electrolyte), then dissolved the mixture by using an ultrasonicator. High purity Ar was used to aerate the Na_5-DTPA solution for 15 min to remove the remaining O_2, and the mixture was added with the same molar quantity of $FeCl_2 \cdot 4H_2O$ as DTPA. Once completely dissolved, the Fe^{2+}-DTPA solution was heated in a water bath at 50°C for 30 min until complete chelation. For example, to configure 1 L 0.1 M Fe^{2+}-DTPA electrolyte, 39.34 g (0.1 mol) DTPA, 20 g (0.5 mol) NaOH, 19.90 g (0.1 mol) $FeCl_2 \cdot 4H_2O$ and 0.8 L deionized water was required. For the $Na_3[Fe(CN)_6]$ electrolyte preparation, the same molar quantity of $Na_3[Fe(CN)_6]$ as Fe^{2+}-DTPA was dissolved in inorganic solution. Twofold NaCl was additional added to balance osmotic pressure. Finally, 10% (in volume) inorganic medium (10✕) and 10% phosphate buffer solution (10✕, pH = 7.0) were added in Fe^{2+}-DTPA or $Na_3[Fe(CN)_6]$ solution to construct the final electrolyte. For the 50% state of charge (SOC) catholyte/anolyte, the same concentrations of Fe^{2+}-DTPA/Fe^{3+}-DTPA and $Na_3[Fe(CN)_6]$/$Na_4[Fe(CN)_6]$ were mixed to be prepared. The pH of all the electrolytes was adjusted to 7.0 with 25 wt.% $NH_3 \cdot H_2O$ and 1 M diluted HCl.

Microorganism and enrichment

The initial FeOB sample was acquired from the rust of iron products exposed to humid conditions. Unlike chemical corrosion, the extracellular polymeric substance (EPS) secreted by microorganisms allows the oxidation products of ferrous iron to be deposited outside the cell in various crystal structures, resulting in a fluffy appearance. The bacterial inoculum needed for enrichment was obtained by vibrating a 0.1 M phosphate buffer solution containing an appropriate amount of bio-oxidized rust.

Microaerobic FeOB were enriched using gradient tubes with $FeCl_2 \cdot 4H_2O$ as the energy source substrate.[51] The bottom layer of iron substrate was composed of 19.90 g/L (0.1 M) $FeCl_2 \cdot 4H_2O$ and 1% agar (wt/vol). The top layer contained (g per liter): NH_4Cl, 0.50; $MgSO_4$, 0.20; $CaCl_2$, 0.10; $NaHCO_3$, 1.20; K_2HPO_4, 0.05 and 0.15% agar (wt/vol), 1 ml/L vitamins and minerals solution were used as supplements. The pH was adjusted to 7.0 by aerating the mixture with CO_2 gas. Both bottom and top layers were sterilized at 121°C for 15 min till the agar completely melted. A gradient tube was fabricated as follows: 1ml bottom layer was added into the anaerobic tube (effective volume 10 ml), after complete solidification, 5 ml top layer was carefully injected to form a semisolid medium. It took 24 h for Fe^{2+} ions to diffuse into the top layer in different concentration levels, and the headspace was filled with air. The inoculum (10 μL) was injected into the top layer evenly for enrichment, then cultured at 30°C in the dark for 15 d. Ultimately, FeOB spontaneously moved to the regions with suitable Fe^{2+} and O_2 concentrations, formed a distinct band of $Fe(OH)_3$.

Reactor configuration

The two-chamber plexiglass reactors were used and the effective volume of both cathode and anode chambers were 120 ml. Between the two chambers, the CMI-7000S (for batch experiments) or Nafion™212 (for GCD experiments) exchange membranes were tightly fixed, membrane area was 25 cm². The membranes were regenerated with 5% H_2SO_4 and 5% H_2O_2 at 80°C for 1 h, and rinsed several times with deionized water. Two graphite electrodes (0.3 ✕ 2.5 ✕ 2.5 cm³) were connected with Pt electrode holders as the cathode and anode, which were pre-processed as follows: the graphite electrodes were first soaked in acetone for 24 h, then immersed in 1 M NaOH and 1 M HCl for 1 h each. They were then rinsed with deionized water, and dried in the oven at 400°C.

After the reactors were assembled, they were washed with chloramine and rinsed several times with deionized water to prevent possible contamination. Ar was vented into the reactors to drain the remaining air before pouring in the electrolyte. Different volumes of the electrolyte for batch experiments (120 ml each) and GCD experiments (100 ml each) were transfused into the reactors through different sterilized hose in an anaerobic environment after filtering through a 0.22 μm microporous membrane. In both the first batch and the GCD experimental cultivation process, FeOB enrichment culture (10%) was introduced into the experimental reactors as inoculum, while no microbial inoculum was added in CK.

Two experimental reactors (R1 and R2) and one control reactor (CK) were operated in batch experiments. For the GCD experiments, only one experimental and one control reactors were needed (GCD and CK, respectively). The anodic chambers were stirred using magnetic stirrers and kept at room temperature.

Experimental procedure

A series of half-battery batch experiments were conducted at 100% SOC to test whether FeOB would enhance the oxidizability of Fe^{2+}-DTPA. The batch experiments could be divided into two periods. In the first period, the concentration of Fe^{2+}-DTPA was gradually increased (0.07–0.1 M), allowing the FeOB to adapt to the environment. The Fe^{2+}-DTPA concentration in the second period was maintained at 0.1 M. The resistors (200 Ω and 10 Ω) were circumscribed to connect the electrodes for electron transfer. Notably, the 200 Ω resistors were used to limit the magnitude of the external current, promoted the microorganisms to grow on the surface of graphite electrodes. A data acquisition card (USB-1252A, Smacq, China) connected to computer recorded the voltage across the resistors in real-time, and converted it into current density at the end of each batch. The potential of bio-anode was monitored with a multimeter (VC890D, Victor, China) at the beginning, 12 h

intervals, and end of each batch. Before and after every batch, sampled each reactor to determine the concentration of Fe^{2+}-DTPA. At the end of each period, the impedance value, power density and polarization statistics of different reactors were measured. Finally, cyclic voltammetry (CV) was used to determine whether FeOB would influence the redox potential of Fe^{2+}-DTPA. It is worth noting that, the electrolyte in reactors would be renewed to 100% SOC condition and stood for 30 min until ion equilibrated before every electrochemical test.

GCD experiments were conducted to measure the battery performance at constant current state, including coulombic, voltagic, energy efficiency and capacity. To increase the theoretical capacity of the Fe^{2+}-DTPA/$[Fe(CN)_6]^{3-}$ flow battery, the reactant concentrations were stepped up (0.1 M–0.5 M) in three periods, each period required three days of cultivation at 3, 10 and 13 mA/cm^2 respectively to allow the microbes to acclimate before formal tests. Higher concentrations of electrolyte resulted in lower coulombic efficiency during battery operation at low current densities, whereas higher current density led to lower voltagic efficiency. Therefore, certain moderate current density gradients were chosen for the tests (3–7 mA/cm^2 for 0.1 M, 10–15 mA/cm^2 for 0.3 M, 13–17 mA/cm^2 for 0.5 M). Every formal test was conducted at 50% SOC with completely renewed electrolytes.

After experiments completion, the microbe-attached graphite electrodes were removed and divided into three pieces for microbial community analysis and scanning electron microscope (SEM) observation. All samples were collected and tested in an anaerobic operating chamber.

QUANTIFICATION AND STATISTICAL ANALYSIS

Fe^{2+}-DTPA concentration was determined by a modified 1,10-phenanthroline colorimetric method at 510 nm, using a spectrophotometer (TU-1810, Persee, China). The equation of coulombic efficiency (η_{cb}) and Fe^{2+}-DTPA oxidation rate (γ_o) are as follows:

$$\eta_{cb} = \frac{\int_0^t I dt}{zFV_a \Delta c} \times 100\% \qquad \text{(Equation 1)}$$

$$\gamma_o = \frac{\Delta c}{c_{in}} \times 100\% \qquad \text{(Equation 2)}$$

where the current (I, A) over a period of time (dt, s) is converted from the potential of resistors, F is the Faraday's constant, Va (L) is the volume of liquid in the anode chamber, z is the number of electrons transferred per molecular, Δc (mol/L) is the change of Fe^{2+}-DTPA concentration and the c_{in} (mol/L) is the initial Fe^{2+}-DTPA concentration.

The polarization and power curves were determined using a series of resistances ranging between 2 kΩ and 10 Ω, using a multi-meter to measure the voltage 5 min after each resistance change. Changes in the anode impedance were measured by electrochemical impedance spectroscopy (EIS) and fitted computationally. The equation of capacitance (C, F) calculated from CV curves is as follow:

$$C = \frac{A}{2k(V_2 - V_1)} \qquad \text{(Equation 3)}$$

where the A (A V) is the integrated area of the CV curve, k is the scan rate (V/s), (V_2-V_1) (V) is the voltage window of test.

The EIS and CV statistics were carried out using an electrochemical workstation (VersaSTAT3, Ametek, America). GCD experiments involved charging and discharging tests in constant current densities, were managed and recorded by a battery formation/grading system (CT-3008, Neware, China). Microbial community analysis was performed by Majorbio Co., China, and SEM pictures were obtained from the Analysis and Measurement Center of Sichuan University, China.

ADDITIONAL RESOURCES

There are no additional resources needed to be declared in this manuscript, additional requests for this can be made by contacting the lead contact.